



High-resolution computational modeling of the current flow in the outer ear during transcutaneous auricular Vagus Nerve Stimulation (taVNS)

Erica Kreisberg ^a, Zeinab Esmaeilpour ^a, Devin Adair ^a, Niranjan Khadka ^b,
Abhishek Datta ^c, Bashar W. Badran ^d, J. Douglas Bremner ^e, Marom Bikson ^{a,*}

^a Department of Biomedical Engineering, The City College of New York, New York, NY, USA

^b Department of Psychiatry, Division of Neuropsychiatry and Neuromodulation, Massachusetts General Hospital and Harvard Medical School, Boston, MA, USA

^c Research and Development, Soterix Medical, New York, USA, The City College of the City University of New York, New York, USA

^d Department of Psychiatry, Medical University of South Carolina, Charleston, SC, USA

^e Departments of Psychiatry & Behavioral Sciences and Radiology, Emory University School of Medicine, And the Atlanta VA Medical Center, Decatur, Atlanta, GA, USA

ARTICLE INFO

Article history:

Received 15 March 2021

Received in revised form

7 September 2021

Accepted 9 September 2021

Available online 10 September 2021

Keywords:

Non-invasive brain stimulation
Transcutaneous auricular vagus nerve stimulation
Auricular branch of the vagus nerve
Computational modelling
Finite element method models
Current flow models

ABSTRACT

Background: Transcutaneous auricular Vagus Nerve Stimulation (taVNS) applies low-intensity electrical current to the ear with the intention of activating the auricular branch of the Vagus nerve. The sensitivity and selectivity of stimulation applied to the ear depends on current flow pattern produced by a given electrode montage (size and placement).

Objective: We compare different electrodes designs for taVNS considering both the predicted peak electric fields (sensitivity) and their spatial distribution (selectivity).

Methods: Based on optimized high-resolution (0.47 mm) T1 and T2 weighted MRI, we developed an anatomical model of the left ear and the surrounding head tissues including brain, CSF/meninges, skull, muscle, blood vessels, fat, cartilage, and skin. The ear was further segmented into 6 regions of interest (ROI) based on various nerve densities: cavum concha, cymba concha, crus of helix, tragus, antitragus, and earlobe. A range of taVNS electrode montages were reproduced spanning varied electrodes sizes and placements over the tragus, cymba concha, earlobe, cavum concha, and crus of helix. Electric field across the ear (from superficial skin to cartilage) for each montage at 1 mA or 2 mA taVNS, assuming an activation threshold of 6.15 V/m, 12.3 V/m or 24.6 V/m was predicted using a Finite element method (FEM). Finally, considering every ROI, we calculated the sensitivity and selectivity of each montage.

Results: Current flow patterns through the ear were highly specific to the electrode montage. Electric field was maximal at the ear regions directly under the electrodes, and for a given total current, increases with decreasing electrode size. Depending on the applied current and nerves threshold, activation may also occur in the regions between multiple anterior surface electrodes. Each considered montage was selective for one or two regions of interest. For example, electrodes across the tragus restricted significant electric field to the tragus. Stimulation across the earlobe restricted significant electric field to the earlobe and the antitragus. Because of this relative selectivity, use of control ear montages in experimental studies, support testing of targeting. Relative targeting was robust across assumptions of activation threshold and tissue properties.

Discussion: Computational models provide additional insight on how details in electrode shape and placement impact sensitivity (how much current is needed) and selectivity (spatial distribution), thereby supporting analysis of existing approaches and optimization of new devices. Our result suggest taVNS current patterns and relative target are robust across individuals, though (variance in) axon morphology was not represented.

© 2021 The Authors. Published by Elsevier Inc. This is an open access article under the CC BY-NC-ND license (<http://creativecommons.org/licenses/by-nc-nd/4.0/>).

* Corresponding author.

E-mail address: bikson@ccny.cuny.edu (M. Bikson).

1. Introduction

The vagus nerve (VN) is the longest cranial nerve in the human body and is highly involved in the regulation of multiple brain and organ systems, making it a target for a wide range of therapies [1]. The auricular branch of the vagus nerve (ABVN), an offshoot branch of the main bundle of the vagus that innervates the ear, has become a compelling stimulation target. Notwithstanding the ear is innervated by additional peripheral and cranial nerves besides the vagus and the nerve densities varies across the ear structures [2], the ABVN presents an easily accessible and well-tolerated means to activate the vagus nerve.

Transcutaneous auricular Vagus Nerve Stimulation (taVNS) is a noninvasive technology that applies low-intensity pulsed electrical current to the ear, activating the ABVN in a deployable and well-tolerated manner [3,4]. Various electrode placement techniques and electrode sizes across the ear are implemented in taVNS with the intention to activate specific nerves, as well as experimental electrode-position control sites to demonstrate specificity. taVNS sensitivity and selectivity are governed by current flow pattern produced by the selected electrode montage (size and placement), with functional outcomes depending further on axon morphology, biophysics, and connectivity. Despite expanding interest in taVNS, the merits of varied electrode montages remain under-specified [5–7].

Current flow modelling of the electrical field generated by various taVNS electrode placements is thus a required step toward understanding of montage-specific subcutaneous nerve activation in the ear. Samoudi et al. [8] and Kuhn et al. [9] developed computational models of percutaneous (needle electrode) auricular Vagus Nerve Stimulation using a two-compartment (tissue and blood vessels) ear model, including explicit nerve stimulation modeling. Here, we develop the first high-resolution multi-compartment MRI-derived transcutaneous (non-invasive electrode) ear stimulation model to predict current flow, considering surface electrode size and position, and predicted electric field across different ROIs. Under a Creative Commons Attribution 4.0 International (CC BY 4.0) license, MRI scans, mask STL files, mesh file, and exemplary simulation files were made available for free download from <https://data.mendeley.com/> (<https://doi.org/10.17632/ydx4d365rw.1>). This facilitates further comparison across montages for sensitivity and selectivity.

2. Methods

2.1. General high-resolution MRI-derived ear model construction and solutions method

We performed a high-resolution T1 and T2 weighted magnetization prepared gradient echo (MPRAGE) MRI scanning of a single healthy adult female's (age: 30 yrs) head using a 3-T Siemens Prisma scanner (Siemens Healthineers, Germany). High resolution (0.47 mm) head scans, highlighting left ear, were acquired using ZOOMit technology (a high-resolution zoomed FOV technique allowing high contrast and less artifact imaging for a region of interest) and an anatomical model of the left ear and the surrounding head tissues including brain/grey-matter, CSF/meninges, skull, muscle, blood vessels, fat, cartilage, and skin were developed using a series of automatic algorithms and manual morphological segmentation filters in Simpleware ScanIP (Synopsys, CA, USA). The ear was further manually segmented into 6 regions of interest (ROI) based on nerve densities as cavum concha, cymba concha, crus of helix, tragus, antitragus, and earlobe (Fig. 1B2). These ROIs were selected for the following reasons: (1) correspondence to canonical anatomical divisions of the ear, (2) nominal targets or control sites

for taVNS, and (3) representation of the ABVN and other nerves within the auricle vary across these regions [6,10–12]. We reproduced a range of taVNS devices (electrode montages) including approaches with various electrode shapes, sizes, and placements over the tragus, cymba concha, earlobe, cavum concha, and crus of the helix.

Electrodes (circular: d = 1 cm, 3 mm, 5 mm, or 8 mm; square: 4 mm × 4 mm or rectangular: 25 mm × 9.5 mm) and gel (thickness: 1 mm) were modeled in COMSOL Multiphysics 5.1 (COMSOL Inc., Burlington, MA) and were manually placed over the target area using Simpleware ScanIP. An adaptive tetrahedral mesh using a built-in voxel-based meshing algorithm was generated, resulting in a refined mesh density that produced less than 1% difference in electric field at the ROIs. The resulting model consisted of > 970 thousand tetrahedral elements with a mean element size of 0.1428 mm³. The final mesh was imported into COMSOL Multiphysics 5.1 to computationally solve for electric field [13].

The corresponding electrical conductivities (σ) for each segmented tissue, electrode, and gel were based on prior literatures [14–16] and were assigned (unless otherwise indicated) as: skull, 0.01 S/m; CSF, 1.65 S/m; cartilage 0.2 S/m; blood vessels, 0.7 S/m; muscle, 0.2 S/m; skin, 0.465 S/m, electrode, 5.8 × 10⁷ S/m; gel, 1.4 S/m; fat, 0.025 S/m; grey-matte, 0.276 S/m; and white matter, 0.126 S/m. In some simulations, the skin (2x standard, 0.93 S/m; or 0.5x standard, 0.2325 S/m) and cartilage (2x standard, 0.4 S/m; or 0.5x standard, 0.1 S/m) conductivities were increased or decreased, as indicated.

For the ear model, normal current density corresponding to 1 mA peak or 2 mA peak taVNS stimulation intensities were applied to the anode electrode while the other electrode was grounded (cathode). The internal boundaries were assigned continuity ($n.(J_1 - J_2) = 0$), and the remaining outer boundaries of the model were insulated ($n.J = 0$). Laplace equation ($\nabla \cdot (\sigma \nabla V) = 0; V = potential, \sigma : electrical conductivity$) was solved to predict the electric field per mA at different ROIs and analyzed the sensitivity and selectivity for each montage. Unless otherwise stated, the peak electric field represents 99th percentile of electric field produced in the region of interest. 99th percentile was calculated in each region of interest by ordering the predicted electric field in all nodes of that region and obtaining the percentile rank to find the 99th percentile value ($n = \frac{P}{100} \times N; n: \text{ordinal rank of a value based on particular percentile}; P: \text{percentile value}; N: \text{number of nodes in the respective ROI}$).

Mean electric field was calculated in each ROI by averaging the predicted electric field in all the nodes of that region ($\mu = \frac{1}{N} \sum_{i=1}^N x_i; \mu: \text{mean electric field}, N: \text{number of nodes in the respective region}, x_i: \text{each predicted electric field value in each node}$). We considered 12.3 V/m as a standard nerve activation threshold [17–21], and further considered halved (6.15 V/m) and doubled (24.6 V/m) activation thresholds.

Electric fields were represented at the surface of the ear and the cartilage to span the full possible area with nerves (terminations). In stimulating results for either 1 mA or 2 mA of applied current, electric fields were plotted to a maximum (either 6.15 V/m or 24.6 V/m) such that areas with electric fields at or above this threshold were red (the maximum on the false color scale). In addition, we plotted each result to each relative maximum to illustrate the full scale of current flow.

For our general comparison, ten taVNS montages were simulated, three of them were considered control montages for montage 1, montage 2, and montage 7 (Fig. 1). These montages were selected based on recently studied and/or commercial availability – and

specifically to cover a range of nominal ear ROI targeting placements.

2.1.1. Montage 1 and montage 1 control

Montage 1 (Fig. 1C1) applied two circular electrodes ($d = 1$ cm each) placed over the tragus. The cathode electrode was positioned over the anterior wall, and the anode electrode was positioned over the posterior outer surface of the ear. Montage 1 Control (Fig. 1C2) applied circular electrodes centered on the anterior surface of the earlobe as the anode electrode whereas the cathode electrode of same dimension was positioned over the posterior surface of the earlobe [3,22].

2.1.2. Montage 2 and montage 2 control

Montage 2 (Fig. 1C3) applied two square electrodes ($4 \text{ mm} \times 4 \text{ mm}$ each) placed over the cymba concha at the anterior surface of the ear, with the anode electrode more rostral, closer to the face than the cathode electrode, and 1 cm apart. In Montage 2 Control (Fig. 1C4) both anode (rostral) and cathode electrodes were centered over the control site (anterior surface of the ear) and 1 cm apart [23,24].

2.1.3. Montage 3

Montage 3 (Fig. 1C5) applied two circular electrodes ($d = 5$ mm each) positioned anteriorly over the cavum concha as the cathode electrode and anode electrode over the cymba concha of the ear [25].

2.1.4. Montage 4

Montage 4 (Fig. 1C6) applied four circular electrodes ($d = 3$ mm each) positioned anteriorly in a crosswise manner with two over the external ear canal as the cathode electrodes, and the other two over the crus of helix and cavum concha area as the anode electrodes [26].

2.1.5. Montage 5

Montage 5 (Fig. 1C7) applied two circular electrodes ($d = 8$ mm each) positioned anterior over the tragus as the cathode electrode and posterior to the first electrode as the anode electrode [22,27].

2.1.6. Montage 6

Montage 6, a test montage (Fig. 1C8), applied two rectangular hydrogel-based electrodes of same dimension ($l: 25 \text{ mm}, w: 9.5 \text{ mm}$; electrode contact area: $l = 13.5 \text{ mm}, w = 9 \text{ mm}$) with the

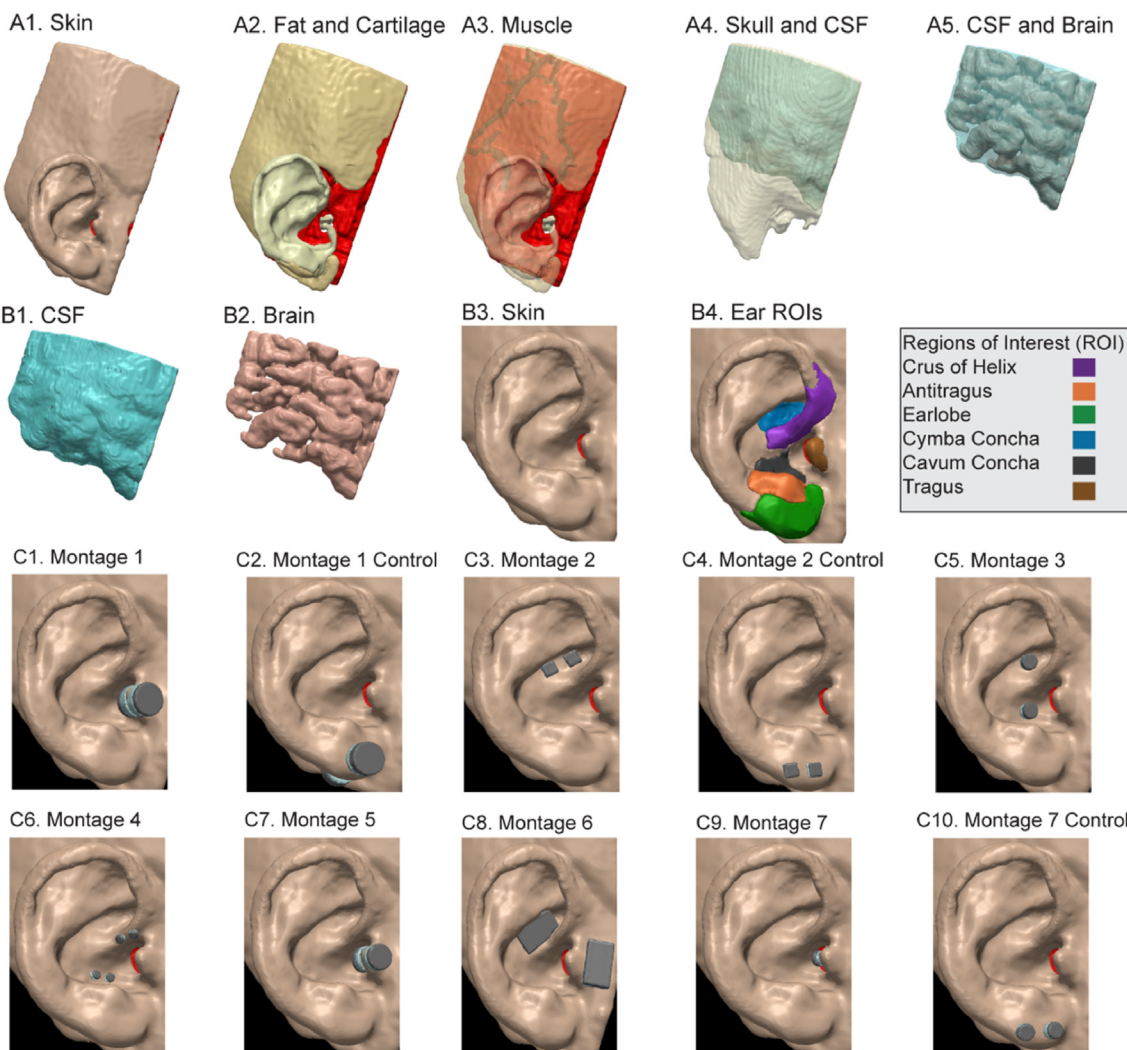


Fig. 1. Segmented anatomy of outer ear, the region of interests (ROIs) of ABVN, and simulated tAVNS montages. A1-A5, B1-B3 represent segmentation of outer ear skin, outer ear cartilage, fat, muscle, blood vessels, CSF, brain/grey-matter, as well as color coded ROIs (B4). C1-C10 indicate montages simulated. (For interpretation of the references to color in this figure legend, the reader is referred to the Web version of this article.)

cathode electrode positioned over the cymba concha and the anode electrode positioned anterior to the tragus.

2.1.7. Montage 7 and montage 7 control

Montage 7 (Fig. 1C9) applied two circular electrodes ($d = 5$ mm each) positioned over the external acoustic meatus, anterior to the tragus and over the interior surface of the outer ear. Electrodes were positioned 5 mm apart, with the anode electrode positioned closer to the inner ear and the cathode electrode positioned more anterior to the tragus. Montage 7 Control (Fig. 1C10) applied two circular electrodes ($d = 5$ mm each) positioned anteriorly over the earlobe where the anode electrode was more rostral, towards the face than the cathode electrode, and were 5 mm apart [28].

Modeling skin as a homogenous layer does not account for the impact of ultrastructures on current flow [16], however, we considered our comparisons across montages and ROIs insensitive to this detail, and do not explicitly model axon stimulation [29]. Our reliance on electric field depends on the quasi-uniform assumption [13,30]. These general assumptions are consistent with comparable prior FEM stimulations of transcutaneous stimulation [9] and establishment of peripheral nerves stimulation thresholds based on electric field [13,31–34]. However, to further verify the insensitivity of model predictions to assumptions about skin properties we implemented a multilayer ear skin model.

2.2. Multilayer ear skin model structure and solutions method

In a separate analysis, we adapted the prior skin current flow model [16] and developed a multi-layer ear skin model comprising epidermis (thickness: 100 μm), dermis (thickness: 2 mm), and cartilage (thickness: 2 cm), to assess the role of skin conductivities and gel parameter in current flow [16] (Fig. 6). The CAD derived model of ear multilayer skin, electrode, and gel were developed in COMSOL Multiphysics 5.1 (COMSOL, MA, USA). The final refined tetrahedral mesh of multi-layer ear skin model consisted of 4,554,989 tetrahedral elements.

The assigned electrical conductivities (σ) were based on prior literature as epidermis: $1.05 \times 10^{-5} \text{ S/m}$ (resistive) or 0.12 S/m (standard); dermis: 0.23 S/m (standard) or $1.05 \times 10^{-5} \text{ S/m}$ (resistive); and cartilage: 0.2 S/m (standard) [35,36]. Three different gel conductivities were considered (σ : 0.001 S/m , 0.1 S/m , and 1.4 S/m). Normal current density corresponding to 1 mA was applied at the top surface of the circular electrode (d : 1 cm; thickness: 1 mm; σ : $5.8 \times 10^7 \text{ S/m}$) and the bottom surface of the skin was grounded (cathode). The internal boundaries were assigned continuity and the remaining external boundaries of the model were insulated. We solved the Laplace equation ($\nabla \cdot (\sigma \nabla V) = 0; V = \text{potential}$, σ : electrical conductivity) under the quasi-static assumption to predict the current flow across the model. Fig. 6 depicts the current flow pattern across different tissue layers and current density distribution below the surface ($\sim 1 \text{ mm}$). Anatomically the nerve fibers in the outer ear are at a depth within the range of 1–1.5 mm [8,12,37]. We averaged current densities sampled from a $1 \text{ cm} \times 1 \text{ cm}$ ROI, located at the edge and the center of the skin surface (under the electrode and gel at $\sim 1 \text{ mm}$ below the top skin surface) for each simulated condition. A non-uniformity current density metric (κ) was defined as the ratio between the averaged current density at the edge (J_{edge}) to the averaged current density at the center (J_{center}) of the skin surface ($\kappa = J_{\text{edge}}/J_{\text{center}}$) for each layer [16] (Fig. 6).

2.3. Underlying modeling assumptions

The approach taken, and so the resulting conclusions, thus depends on several assumptions:

- 1) Tissue is segmented into nine or three homogenous isotropic regions representing a single subject. For example, blood vessels are represented [5,38].
- 2) Absence of capacitive tissue effects (permittivity) supported by the frequency range of taVNS [27] and absence of adaptive (current-dependent) conductivity supported by the low taVNS intensity [39]. Predicted tissue electric fields are thus linear with applied current; in post-processing, we applied three (non-linear) electric field thresholds.
- 3) Nerve stimulation is predicted by electric field magnitude supported by the response of the axon terminal (end organs) to electric field [40–43] and the general quasi-uniform assumption [13,30,31,44]. Analysis is further aggregated into ROIs based on prior axon mapping studies. Such an approach neglects stimulation of axons of passage (i.e., passing through but not terminating in a ROI) or axon-type specific responsiveness. The latter is mitigated by the considered robustness of conclusions across assumed thresholds.
- 4) Temporal dynamics (frequency, pulse duration) are not considered, which would require explicit representation of axon morphology and membrane biophysics – and so depend on the accuracy of such parameterization. The functional significance (e.g., cortical innervation) of ROI specific axon stimulation is not considered.

Our analysis and conclusions thus derive from the general assumption that, for each taVNS montage, the stimulation of axons in each ROI depends on significant (threshold) local current density. Conversely, axons in the ROIs with minimal current density will not be stimulated; a notion that is robust to the consideration of details such as axon morphology or presence of vasculature. A corollary is that taVNS montages that produce distinct current flow patterns result in a unique axon stimulation. For each taVNS montage, sensitivity is defined by the ROI electric field per mA applied, which is further categorized into four stratifications based on thresholds. Selectivity is defined by the ratio of electric field in the peak ROI compared to other ROIs. Relative selectivity considers selectivity across taVNS montages, including using the four stratifications based on thresholds.

3. Results

3.1. General high-resolution MRI-derived ear model results

The current flow pattern through the ear was highly specific to the electrode montage. Generally, electric fields were maximal in ear regions directly under the electrodes, and for a given total applied current increased with decreasing electrode size (i.e., peak tissue electric field increased with increasing electrode current density). Depending on the applied current and nerves activation threshold, activation might also occur in the regions between electrodes in montages with multiple anterior surface electrodes. As the goal of this study was to consider the inter-montage difference, we considered electric field per 1 mA and 2 mA on a fixed scale across the montages (Column 3/4 and 5/6 in Figs. 2 and 3) or on full scale (Column 7/8 in Figs. 2 and 3), as well as analyzed targeting across four rankings (Figs. 4 and 5). When plotting results for 1 or 2 mA applied on a uniform scale, the electric field scale of 12.3 V/m or 6.15 V/m (where all values at or above these values were in red) can be understood as representing these activation thresholds. Note, as a result of simulation linearity, a threshold of 6.15 V/m at 1 mA is equivalent to a threshold of 12.3 V/m at 2 mA (Column 5/6 in Figs. 2 and 3; Figs. 4 and 5: cyan rank), and a threshold of 12.3 V/m at 1 mA is equivalent to a threshold of 24.6 V/m at 2 mA (Figs. 4 and 5: orange rank).

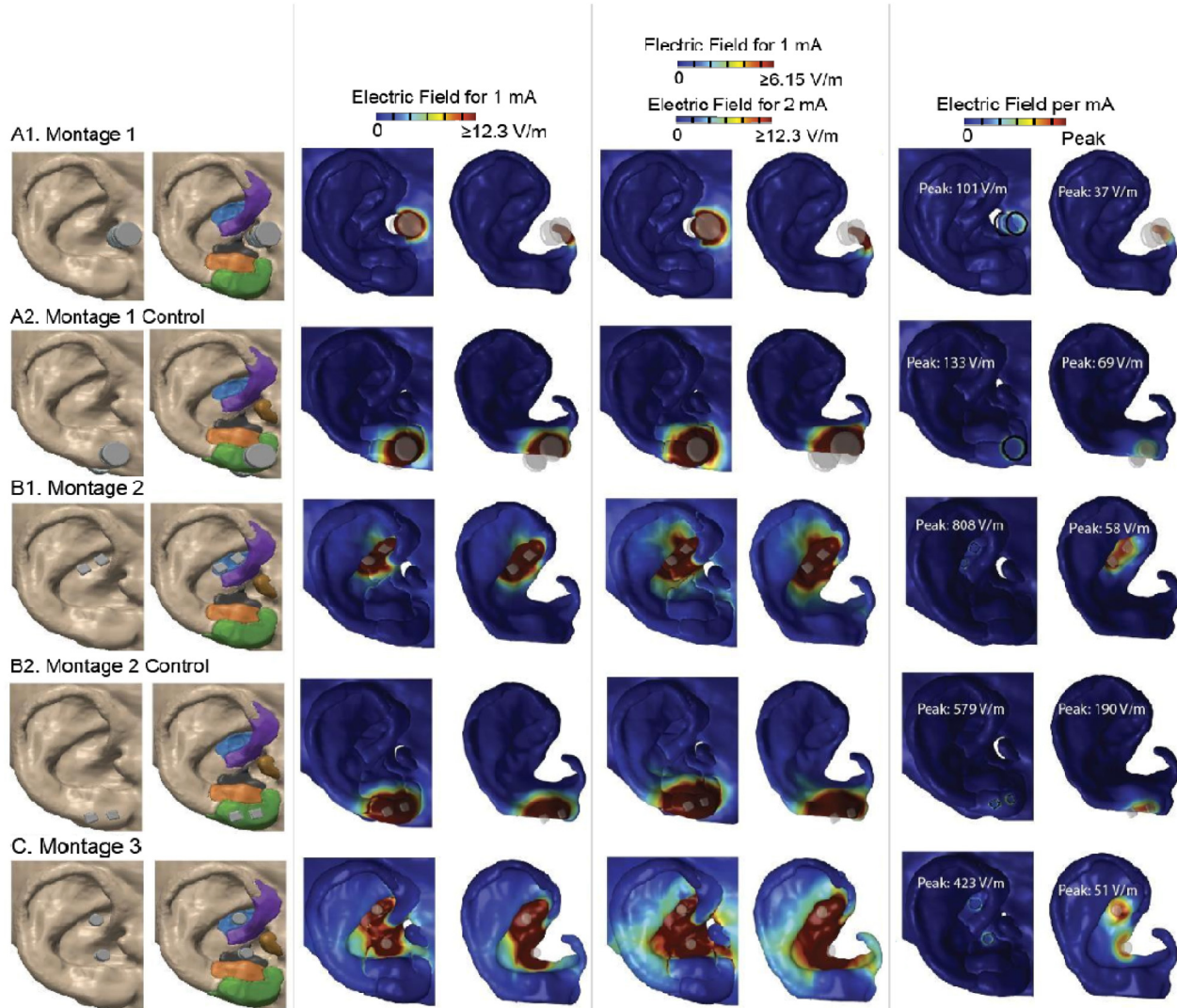


Fig. 2. Predicted electric field distribution at the skin and cartilage for five tAVNS montages (Montage 1, Montage 1 control, Montage 2, Montage 2 control, and Montage 3). Electrode positioning for each montage without (column 1) and with (column 2) color coded ROIs for ABVN. For an applied current of 1 mA and an electric field scale (threshold) to 12.3 V/m, the electric field predicted on the ear (column 3) and cartilage (column 4). For an applied current of 2 mA and an electric field scale (threshold) to 12.3 V/m, the electric field predicted on the ear (column 5) and cartilage (column 6). The electric field per mA of applied current on an absolute scale (peak for each simulation as indicated) on ear (column 7) and cartilage (column 8). Across simulation, peak electric field are under the electrode as well as, for montages with multiple electrodes on the anterior ear surface between electrodes. (For interpretation of the references to color in this figure legend, the reader is referred to the Web version of this article.)

Montage 1 (Fig. 2A1) produced the maximum electric field in the tragus region (Peak = 56.02 V/m; mean \pm SD = 21.12 ± 9.41 V/m) while other ROIs received significantly less electric field (mean < 0.1 V/m) (Fig. 4). Montage 1 control (Fig. 2A2) produced maximum peak and mean electric field in the earlobe (Peak = 57.78 V/m, mean \pm SD = 15.75 ± 11.75 V/m) and antitragus (Peak = 51.15 V/m, mean \pm SD = 7.02 ± 10.74 V/m) regions (Fig. 4). Because of their relative selectivity for the tragus, our results support the testing of montage 1 with a montage 1 control.

Montage 2 (Fig. 2B1) produced the maximum peak and mean electric field in the cymba concha region (Peak = 307.23 V/m, mean \pm SD = 55.75 ± 57.92 V/m) and in the crus of the helix region (Peak = 201.40 V/m, mean \pm SD = 11.42 ± 47.04 V/m) while other ROIs received significantly less electric field (mean < 2.1 V/m) (Fig. 4). Montage 2 control (Fig. 2B2) produced maximum peak and mean electric field in the earlobe (Peak = 245.06 V/m, mean \pm SD = 27.47 ± 47.79 V/m) and antitragus (Peak = 34.00 V/m,

mean \pm SD = 7.46 ± 7.45 V/m) regions, respectively (Fig. 4). Because of their relative selectivity for the cyma concha, our results support the testing of montage 2 with a montage 2 control.

Montage 3 (Fig. 2C) produced the maximum peak and mean electric field in the cyma concha region (Peak = 153.21 V/m, mean \pm SD = 27.68 ± 29.85 V/m) and in the cavum concha region (Peak = 157.64 V/m, mean \pm SD = 17.10 ± 25.40 V/m) while other ROIs received significantly less electric field (mean \leq 6.9 V/m) (Fig. 4). Montage 4 (Fig. 3A) produced the maximum peak and mean electric field in the crus of the helix region (Peak = 387.55 V/m, mean \pm SD = 30.54 ± 74.16 V/m) and in the cavum concha region (Peak = 306.47 V/m, mean \pm SD = 28.52 ± 55.95 V/m) while other ROIs received significantly less electric field (mean < 1.9 V/m) (Fig. 4).

Montage 5 (Fig. 3B) produced the maximum peak and mean electric field in the tragus region (Peak = 114.70 V/m, mean \pm SD = 32.59 ± 25.16 V/m) while other ROIs received

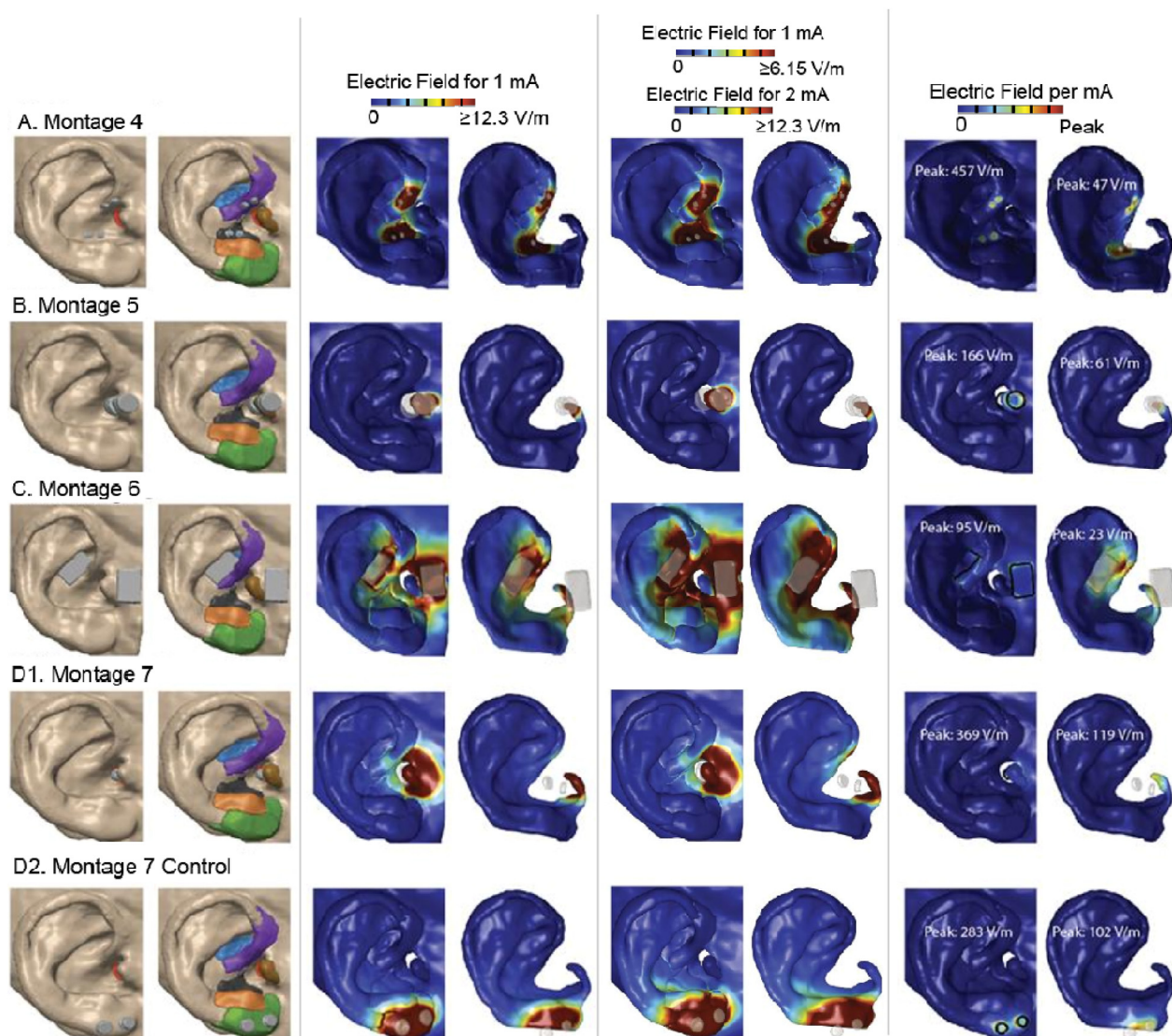


Fig. 3. Predicted electric field distribution at the skin and cartilage for five tAVNS montages (Montage 4, Montage 5, Montage 6, Montage 7, and Montage 7 control). Electrode positioning for each montage without (column 1) and with (column 2) color coded ROIs for ABVN. For an applied current of 1 mA and an electric field scale (threshold) to 12.3 V/m, the electric field predicted on the ear (column 3) and cartilage (column 4). For an applied current of 2 mA and an electric field scale (threshold) to 6.15 V/m or equivalent for an applied current on an absolute scale (peak for each simulation as indicated) on ear (column 5) and cartilage (column 6). The electric field per mA of applied current as well as, for montages with multiple electrodes on the anterior ear surface between electrodes. (For interpretation of the references to color in this figure legend, the reader is referred to the Web version of this article.)

significantly less electric field (mean < 0.04 V/m) (Fig. 4). Montage 6 (Fig. 3C) produced the maximum peak and mean electric field in the cymba concha region (Peak = 26.10 V/m, mean \pm SD = 7.62 ± 4.51 V/m), in the crus of the helix region (Peak = 39.96 V/m, mean \pm SD = 7.06 ± 7.38 V/m), and in the tragus (Peak = 30.46 V/m, mean \pm SD = 6.12 ± 5.88 V/m) (Fig. 4).

Montage 7 (Fig. 3D1) produced the maximum peak and mean electric field in the tragus region (Peak = 253.29 V/m, mean \pm SD = 69.39 ± 40.59 V/m) while other ROIs received significantly less electric field (mean < 1.2 V/m) (Fig. 4). Montage 7 control (Fig. 3D2) produced maximum peak and mean electric field in earlobe (Peak = 159.90 V/m, mean \pm SD = 21.13 ± 28.36 V/m) and antitragus (Peak = 31.05 V/m, mean \pm SD = 7.53 ± 7.16 V/m) regions (Fig. 4). Because of their relative selectivity for the tragus and external acoustic meatus, our results support the testing of montage 7 with a montage 7 control.

Across all the models, montage 5 and 1 produced the most relatively selective current flow pattern (i.e., higher ratio of peak region/other ROIs) and montage 6 produced the most relatively diffused electric field across considered ROIs.

We conducted a sensitivity analysis of each montage by doubling or halving either the ear skin or cartilage conductivities, compared to the standard model (Fig. 5). Each montage thus has four additional tissue conductivity permutations to the standard conductivity model: standard conductivity (A), 2x standard skin conductivity (B), 0.5x standard skin conductivity (C); 2x standard cartilage conductivity (D), and 0.5x standard cartilage conductivity (E). Relative targeting rank order was tabulated based on four electric field ranges (color coded) for each montage and conductivity permutation. The electric field ranges are specified based on varied applied currents (1 mA) and neuron activation thresholds (6.15 V/m, 12.3 V/m, 24.6 V/m) to further consider robustness of

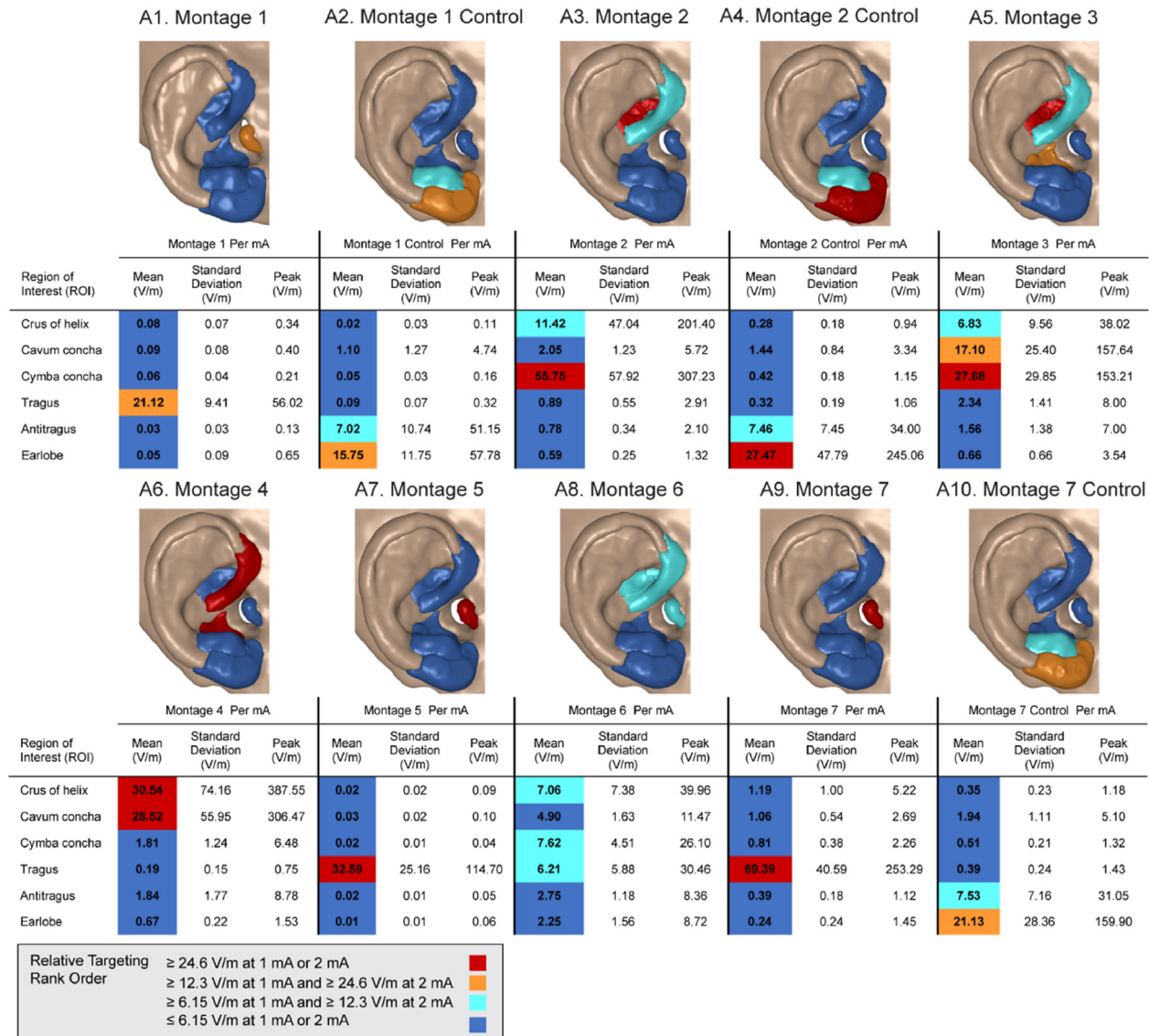


Fig. 4. Predicted electric fields distribution for each ROI, with relative ranking, across taVNS montages simulated. Mean, standard deviation, and peak electric field (99th percentile) are reported. Each mean is categorized according to a relative ranking (see key) that is color coded (from the most to least sensitive: red, orange, cyan, dark blue) applied to both the table and ear ROI plots. The color code itself is represented for various applied current (1 or 2 mA) and nerve activation thresholds (6.15 V/m, 12.3 V/m, 24.6 V/m) to further address robustness on relative targeting predictions. Electric field categories are dark blue: $\leq 6.15 \text{ V/m at } 1 \text{ mA or } 2 \text{ mA}$ (indicating the lowest predicted activation under any assumptions); cyan: $\geq 6.15 \text{ V/m at } 1 \text{ mA and } \geq 12.3 \text{ V/m at } 2 \text{ mA}$; orange: $\geq 12.3 \text{ V/m at } 1 \text{ mA and } \geq 24.6 \text{ V/m at } 2 \text{ mA}$; and red: $\geq 24.6 \text{ V/m at } 1 \text{ mA or } 2 \text{ mA}$ (indicating the highest predicted activation under any assumptions). (For interpretation of the references to color in this figure legend, the reader is referred to the Web version of this article.)

model predictions. Predictions of relative targeting (ranking) were preserved across model conductivity permutations. In no case did the rank order between ROIs change with tissue conductivity for a given ROI. Similarly, in no case did rank order between montages change with tissue conductivity for a given ROI. This robustness supports study conclusions on relative targeting between taVNS montages.

Generally, increases in electric field (and so ranges) is expected when skin conductivity decreases. In general, model conclusions (targeting) were robust across conductivity or threshold assumptions. For example, Montage 1 produced significant electric fields only in the tragus regardless of assumptions. Montage 2 consistently produced highest electric fields in the earlobe with some activation in the antitragus depending on assumptions.

3.1.1. Multilayer ear skin model structure results

The multilayer ear skin models predicted current flow patterns ~1 mm below surface of skin (where nerve fibers run; [8,12,37]) for a given gel conductivity and skin tissue conductivities (Fig. 6). Specifically, the current flow in all simulated conditions followed a trapezoidal pattern.

For the multilayer ear skin models, the non-uniformity current density metric (κ) was calculated for the current flow distribution ~1 mm below surface of skin surface for each permutation of gel and skin tissue conductivities. Across gel conductivities, the non-uniformity metrics (κ) for resistive epidermis and standard conductivity dermis and cartilage (Fig. 6A) ranged from 0.35 to 0.45. For the standard conductivity epidermis, dermis, and cartilage (Fig. 6B), the κ values ranged from 0.37 to 0.62, across gel conductivities. For the resistive epidermis, dermis, and standard

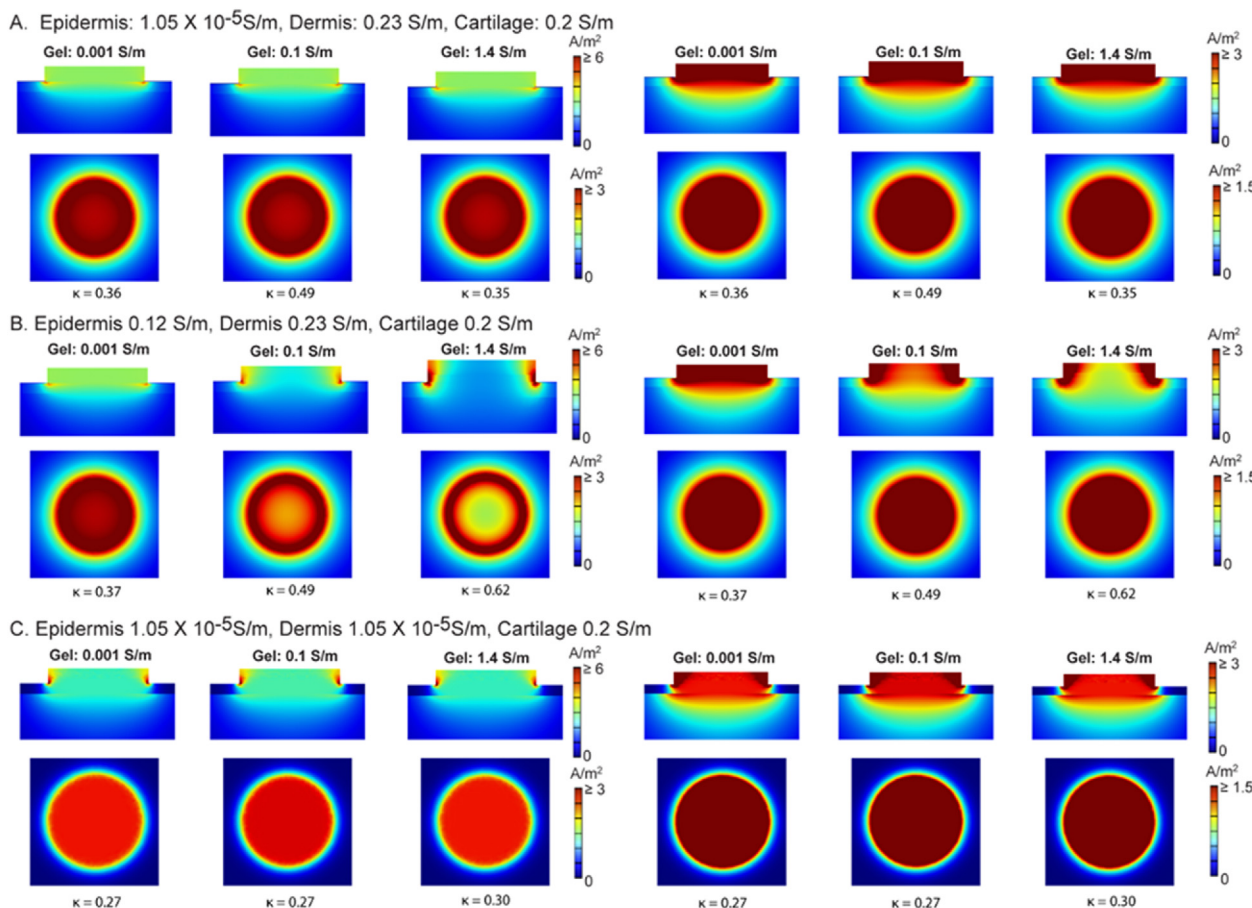
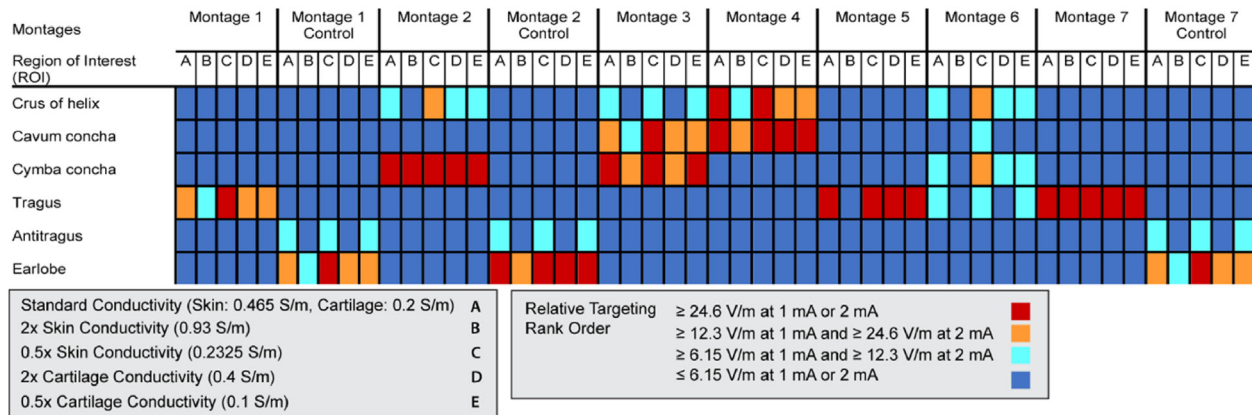


Fig. 6. Multilayer ear skin model and predicted current flow pattern across varied assumed electrode and tissue conductivities. The top panels of A, B, and C show cross-section view of current density distribution across skin layers whereas the bottom panels of A, B, and C show current density distribution at ~1 mm below the top skin surface and the corresponding non-uniformity current density metric (κ ; see Methods). The predicted current density for each simulation is shown in different color scales: top left panels (skin cross-section): $0 - \geq 6 \text{ A/m}^2$; bottom left (skin-surface): $0 - \geq 3 \text{ A/m}^2$; top right (skin cross-section): $0 - \geq 3 \text{ A/m}^2$; bottom right (skin-surface): $0 - \geq 1.5 \text{ A/m}^2$. (A) Shows predicted current densities at the skin layers for resistive epidermis (1.05×10^{-5} S/m) with standard dermis (0.23 S/m), and standard cartilage (0.2 S/m) conductivities and three gel conductivities: 0.001 S/m, 0.1 S/m, and 1.4 S/m, respectively. (B) Shows predicted current densities at the skin layers for conductive epidermis (0.12 S/m), and standard dermis (0.23 S/m) and cartilage conductivities (0.2 S/m), and different gel conductivities. (C) Shows predicted current densities at the skin layers for resistive epidermis (1.05×10^{-5} S/m), and resistive dermis (1.05×10^{-5} S/m), with standard cartilage conductivity (0.2 S/m), and three gel conductivities. Across simulated conditions, the current density non-uniformity metrics ranged from 0.27 to 0.62. (For interpretation of the references to color in this figure legend, the reader is referred to the Web version of this article.)

conductivity cartilage, the κ values ranged from 0.27 to 0.30, across gel conductivities (Fig. 6C).

4. Discussion

We developed the first high-resolution models of taVNS and compared across 10 general montages to determine the impact of electrode design on resulting current flow. All codes/raw files including the MRI scans, mask STL files, and mesh files for the investigated montages are freely available under Creative Commons Attribution-Noncommercial International License (<https://doi.org/10.17632/ydx4d365rw.1>). The distribution of current flow governed the sensitivity and selectivity of ABVN stimulation. We showed an evident difference across montages that should inform the selection of electrode design for specific applications and experimental designs.

Across all the models, montage 5 and 1 generated the most relatively focal electric field (i.e., higher ratio of peak region/other ROIs) in the nominal target – this reflects as much the underlying anatomy as the specific electrode design. Montage 6 produced the most relatively diffused electric field across ROIs which may be advantageous when the target is not well defined or multi-faceted. We show that common controls used for specific montages do steer current to unique regions (albeit which themselves have a unique nerve representations) - but more generally any of these considered montages can be used as controls for each-other in studies aiming to show specificity in target engagement.

Computational models of current flow are standard tools to inform how selecting electrode montage impacts sensitivity and selectivity of nerve stimulation [32,45–47]. Despite the rapid increase in applications and testing of taVNS, as well as other forms of ear neuromodulation, most devices are designed based on heuristic rules (e.g., place electrodes “over” a target). In contrast, more attention has been given to considering the temporal waveform (pulse shape, frequency) of taVNS [48] including sophisticated closed-loop approaches [38,49]. The taVNS current flow models developed here, thus have broad applicability in the analysis (and comparison) of existing approaches and ongoing device optimization.

The present study compared across taVNS montages in a single exemplary subject, as typical in studies developing new neuromodulation modeling pipelines and when the goal is to make gross inter-montage comparisons [14,46,50–53]. None-the-less, the importance of individualized dosimetry in other neuromodulation domains [54–59] warrants discussion for the taVNS. Our result showed that across montages taVNS induced current flow was restricted between the electrodes (Figs. 2 and 3) resulting in a categorical targeting (Fig. 4), that was moreover insensitive to model assumptions (Fig. 5). A secondary modeling analysis confirmed that the taVNS induced current density pattern in the ear skin was largely insensitive to (individual) skin properties (Fig. 6). Our result thus suggested that current flow patterns in the ear would be consistent across individuals, with peak intensities governed by an average electrode current density. Notwithstanding this prediction, when new electrode designs or unusual anatomy (e.g., newborns) is considered, specialized models can be developed.

The applications of taVNS consider two complementary pathways, “downstream” stimulation of peripheral organs (bio-electronic medicine) and “upstream” stimulation of the brain [1]. The former focuses on parasympathetic markers of target engagement [48,60] while the latter considers direct modulation of cognition. In both cases, deep brain nuclei serve as junctions and are the target of taVNS supported by neuroimaging studies [9,46,47,57–59,61]. While distinguishing “upstream” vs

“downstream” effects depend on underlying brain networks, experimentally characterizing these effects depends on first understanding montage-specific current flow.

Direct prediction of sub-cellular level polarization and action potential threshold can be computed using well-established pipelines [43,62–64], yet the accuracy (value) of resulting predictions depends on precise representation of membrane biophysics and morphology (branching) as well as meso-scale anatomy [47,65] such as fascicle [66–68] and skin ultra-structure [16,29,69]. This detailed information for ABVN axon-specific physics, density/distribution including branching structure, or fascicles cyto-architecture are lacking and debated [1,19,54], and in key regards wholly absent (e.g., tertiary branching structure). However, it is known that axon terminations are most sensitive to polarization [42,61,70], with the ABVN (and other nerve) end-organs at the ear (taVNS ROIs). Specifically, terminals polarize directly with electric field intensity [40,71]. Therefore, practical studies and regulatory standards for peripheral nerve activation rely on the electric field threshold values [13,31–34], as we referenced. As such, these electric fields represent a conservative basis for predicting taVNS activation. Besides this, the goal of this report was to consider relative activation across montages; importantly, our conclusions were robust across assumptions of electric field threshold (e.g., 1 mA or 2 mA, 12.3 V/m or 6.15 V/m threshold, Figs. 2, 3 and 5).

taVNS clinical applications are broad and expanding including improving oromotor function in newborns [72,73], treatment of neurological and psychiatric disorders [26,74,75], pain or fatigue [76–79], addiction [80], neurorehabilitation [81,82], general measures of quality of life [83], and management of disorders related to COVID-19 [82,33]. It seems important to consider how taVNS montage should be optimized for each application.

While there have been significant developments in waveform optimization [48] including closed-loop stimulation [46,57,84] and TMS-synchronized stimulation [85], there have been relatively limited optimization of electrode montage. taVNS studies testing more than one (contrasting) electrode montages did so as “control” sites [86,87,84]. Our modeling results support the use of an earlobe electrode as an active control. Yakunina et al. [88] using custom electrodes, compared four stimulation locations in the ear: the inner tragus, inferoposterior wall of the ear canal, cymba conchae, all with a return electrode on the outer surface of the tragus, as well as an earlobe location as a sham. Using small bipolar electrodes, Keute et al (2021) [89], reported that effects on heart rate did not vary between tragus and cymba electrode location [89].

In addition to the electric field patterns/targeting (considered here) and waveform, other considerations impact the final selection of a particular taVNS device. For instance, the need for extended duration (>1 h) applications or where significant movement is expected may dictate a designed optimized for reliable fit or uses in remote settings (e.g., home) may dictate designs that are more reliably self-applied [90]. Notwithstanding these practical considerations, it is stimulation dose that governs neuromodulation [1,91] so current flow models should inform any taVNS effort.

The International Consensus Based Review and Recommendations for Minimum Reporting Standards in Research on Transcutaneous Vagus Nerve Stimulation (Version 2020) identified limitations in the taVNS field [92] such as the lack of a definitive description of a dose, validation of a control site, securing optimal stimulation parameters, and ambiguity surrounding ear and tissue anatomy of the ABVN. Responsive to these concerns, our simulations considered taVNS with detailed dose and considered the impact of dose parameters (electrode position, size, and current intensity), explicitly indicated the value of control sites, serving as a

necessary step (though not complete in the absence of detailed axon tractography) toward addressing nerve targeting.

5. Conclusions

Despite encouraging trials, there are discrepancies among the taVNS results. Difference in electrode montage, including “incidental” differences between approaches that nominally target the same region (e.g., varied electrode size or position for the same nominal target) is one source of variability. Computational models provide additional insight on how details of electrode shape and placement impact sensitivity (how much current is needed) and selectivity, thereby supporting analysis of existing approaches and optimization of new devices. Further iterations of this modeling pipeline can consider individual differences (e.g., based on subject-specific images) and incorporate neurophysiological response (e.g., axon firing simulations).

CRediT authorship contribution statement

Erica Kreisberg: Data curation, Methodology, Visualization, Writing – original draft, Writing – review & editing. **Zeinab Esmaeilpour:** Data curation, Methodology, Visualization, Writing – original draft, Writing – review & editing. **Devin Adair:** Visualization, Writing – original draft. **Niranjan Khadka:** Data curation, Methodology, Visualization, Writing – review & editing. **Abhishek Datta:** Methodology, Writing – original draft. **Bashar W. Badran:** Methodology, Writing – original draft. **J. Douglas Bremner:** Methodology, Writing – original draft. **Marom Bikson:** Conceptualization, Visualization, Project administration, Writing – original draft, Writing – review & editing.

Declaration of competing interest

The City University of New York (CUNY) has IP on neuro-stimulation systems and methods with authors NK and MB as inventors. MB has equity in Soterix Medical. MB serves on the scientific advisory boards, received grants, and/or consults for Boston Scientific, Biovisics, Mecta, Halo Neuroscience, and GlaxoSmithKline Inc., and Google X. BB is listed as an inventor on brain stimulation patents assigned to the Medical University of South Carolina and has equity in Bodhi NeuroTech Inc. BB is supported by the following grants: P20GM109040, P2C HD086844, P2C HD086844, P2CHD086844, P50 DA046373. JDB receives grant support from the VA Merit Review I01 RX003418 and NIH R01 MH120262, R01 HL109413, UC3 DA048502 and devices from ElectroCore LLC. AD is supported by the following grants: 75 N95020C00024 and HR00119S0035-10.

Acknowledgments

Source(s) of financial support: This study was partially funded by grants to MB from the National Institutes of Health: NIH-NIDA UG3DA048502, NIH-NIGMS T34GM137858, NIH-NINDS 1R01NS112996, NIH-NINDS 1R01NS101362, NIH-NIMH 1R01MH111896, and NIH-NINDS 1R01NS095123.

References

- [1] Adair D, Truong D, Esmaeilpour Z, Gebodh N, Borges H, Ho L, Bremner JD, Badran BW, Napadow V, Clark VP. Electrical stimulation of cranial nerves in cognition and disease. *Brain Stimul.* 2020;13:717–50.
- [2] Butt MF, Albusoda A, Farmer AD, Aziz Q. The anatomical basis for transcutaneous auricular vagus nerve stimulation. *J Anat* 2020;236:588–611.
- [3] Badran BW, Alfred BY, Adair D, Mappin G, DeVries WH, Jenkins DD, et al. Laboratory administration of transcutaneous auricular vagus nerve stimulation (taVNS): technique, targeting, and considerations. *J. Vis. Exp.* 2019;143: 10.3791–58984.
- [4] Wang Y, Li S-Y, Wang D, Wu M-Z, He J-K, Zhang J-L, Zhao B, Hou L-W, Wang J-Y, Wang L. Transcutaneous auricular vagus nerve stimulation: from concept to application. *Neurosci Bull* 2020;1–10.
- [5] Badran BW, Brown JC, Dowdle LT, Mithoefer OJ, LaBate NT, Coatsworth J, DeVries WH, Austelle CW, McTeague LM, Yu A. Tragus or cymba conchae? Investigating the anatomical foundation of transcutaneous auricular vagus nerve stimulation (taVNS). *Brain Stimul.* 2018;11:947.
- [6] Kaniusas E, Kampusch S, Tittgemeyer M, Panetsos F, Gines RF, Papa M, Kiss A, Podesser B, Cassara AM, Tanghe E. Current directions in the auricular vagus nerve stimulation I—a physiological perspective. *Front Neurosci* 2019;13:854.
- [7] Yap JY, Keatch C, Lambert E, Woods W, Stoddart PR, Kameneva T. Critical review of transcutaneous vagus nerve stimulation: challenges for translation to clinical practice. *Front Neurosci* 2020;14.
- [8] Samoudi AM, Kampusch S, Tanghe E, Széles JC, Martens L, Kaniusas E, Joseph W. Numerical modeling of percutaneous auricular vagus nerve stimulation: a realistic 3D model to evaluate sensitivity of neural activation to electrode position. *Med Biol Eng Comput* 2017;55:1763–72.
- [9] Kuhn A, Keller T, Lawrence M, Morari M. A model for transcutaneous current stimulation: simulations and experiments. *Med Biol Eng Comput* 2009;47: 279–89.
- [10] Peuker ET, Filler TJ. The nerve supply of the human auricle. *ClinAnat* 2002;15: 35–7.
- [11] Safi S, Ellrich J, Neuhuber W. Myelinated axons in the auricular branch of the human vagus nerve. *Anat Rec* 2016;299:1184–91.
- [12] Samoudi AM, Kampusch S, Tanghe E, Széles JC, Martens L, Kaniusas E, Joseph W. Sensitivity analysis of a numerical model for percutaneous auricular vagus nerve stimulation. *Appl Sci* 2019;9(3):540.
- [13] Bikson M, Truong DQ, Mourdoukoutas AP, Aboseria M, Khadka N, Adair D, Rahman A. Modeling sequence and quasi-uniform assumption in computational neurostimulation. *Prog Brain Res* 2015;222:1–23.
- [14] Datta A, Bansal V, Diaz J, Patel J, Reato D, Bikson M. Gyri-precise head model of transcranial direct current stimulation: improved spatial focality using a ring electrode versus conventional rectangular pad. *Brain Stimul.* 2009;2:201–7. e201.
- [15] Datta A, Dmochowski JP, Guleyupoglu B, Bikson M, Fregni F. Cranial electrotherapy stimulation and transcranial pulsed current stimulation: a computer based high-resolution modeling study. *Neuroimage* 2013;65:280–7.
- [16] Khadka N, Bikson M. Role of skin tissue layers and ultra-structure in transcutaneous electrical stimulation including tDCS. *Phys Med Biol* 2020b;65: 225018.
- [17] Havel WJ, Nyenhuys JA, Bourland JD, Foster KS, Geddes LA, Gruber GP, Waniger MS, Schaefer DJ. Comparison of rectangular and damped sinusoidal db/dt waveforms in magnetic stimulation. *IEEE Trans Magn* 1997;33(5): 4269–71.
- [18] IEEE. IEEE standard for safety levels with respect to human exposure to electric, magnetic, and electromagnetic fields, 0 Hz to 300 GHz. IEEE. IEEE Std C95; 2019. p. 91–2019. 2011–2312.
- [19] Reilly JP. Maximum pulsed electromagnetic field limits based on peripheral nerve stimulation: application to IEEE/ANSI C95.1 Electromagnetic Field Standards. *IEEE (Inst Electr Electron Eng) Trans Biomed Eng* 1998;45(1): 137–41.
- [20] Reilly JP, Diamant AM. Electrostimulation: theory, applications and computational model. Boston, MA: Artech House; 2011.
- [21] Sweeney JD. “A theoretical analysis of the “let-go” phenomenon. *IEEE (Inst Electr Electron Eng) Trans Biomed Eng* 1993;40(12):1335–8.
- [22] Adair D, Truong DQ, Ho L, Badran BW, Borges H, Bikson M. How to modulate cognition with cranial nerve stimulation? *Brain Stimul.* 2019;12:E42–3.
- [23] Keute M, Boehler L, Ruhnau P, Heinze H-J, Zaehle T. Transcutaneous vagus nerve stimulation (tVNS) and the dynamics of visual bistable perception. *Front Neurosci* 2019;13:227.
- [24] Keute M, Ruhnau P, Heinze H-J, Zaehle T. Behavioral and electrophysiological evidence for GABAergic modulation through transcutaneous vagus nerve stimulation. *Clin Neurophysiol* 2018;129:1789–95.
- [25] He W, Jing X, Wang X, Rong P, Li L, Shi H, Shang H, Wang Y, Zhang J, Zhu B. Transcutaneous auricular vagus nerve stimulation as a complementary therapy for pediatric epilepsy: a pilot trial. *Epilepsy Behav* 2013;28:343–6.
- [26] Hein E, Nowak M, Kiess O, Biermann T, Bayerlein K, Kornhuber J, Kraus T. Auricular transcutaneous electrical nerve stimulation in depressed patients: a randomized controlled pilot study. *J Neural Transm* 2013;120:821–7.
- [27] Bossetti CA, Birdno MJ, Grill WM. Analysis of the quasi-static approximation for calculating potentials generated by neural stimulation. *J Neural Eng* 2008 Mar;5(1):44–53.
- [28] Capone F, Assenza G, Di Pino G, Musumeci G, Ranieri F, Florio L, Barbato C, Di Lazzaro V. The effect of transcutaneous vagus nerve stimulation on cortical excitability. *J Neural Transm* 2015;122:679–85.
- [29] Zhu K, Li L, Wei X, Sui X. A 3D computational model of transcutaneous electrical nerve stimulation for estimating A β tactile nerve fiber excitability. *Front Neurosci* 2017;11:250.

- [30] Khadka N, Truong DQ, Williams P, Martin JH, Bikson M. The quasi-uniform assumption for spinal cord stimulation translational research. *J Neurosci Methods* 2019;328:108446.
- [31] Bikson M, Dmochowski J, Rahman A. The "quasi-uniform" assumption in animal and computational models of non-invasive electrical stimulation. *Brain Stimul* 2013 Jul;6(4):704–5.
- [32] Bikson M, Rahman A, Datta A, Fregni F, Merabet L. High-resolution modeling assisted design of customized and individualized transcranial direct current stimulation protocols. *Neuromodulation: Technol. Neural Interface* 2012;15:306–15.
- [33] Boezaart AP, Botha DA. Treatment of stage 3 COVID-19 with transcutaneous auricular vagus nerve stimulation drastically reduces interleukin-6 blood levels: a report on two cases. *Neuromodulation: J Int Neuromod Soc* 2020;24(1):166–7.
- [34] Borges U, Pfaffenstiel M, Tsukahara J, Laborde S, Klatt S, Raab M. Transcutaneous vagus nerve stimulation via tragus or cymba conchae: are its psychophysiological effects dependent on the stimulation area? *Int J Psychophysiol* 2021 Mar;161:64–75.
- [35] Chopra K, Calva D, Sosin M, Tadisina KK, Banda A, De La Cruz C, Chaudhry MR, Legesse T, Drachenberg CB, Manson PN, Christy MR. A comprehensive examination of topographic thickness of skin in the human face. *Aesthetic Surg J* 2015 Nov;35(8):1007–13.
- [36] Khadka N, Bikson M. Neurocapillary-modulation. *Neuromodulation* 2020 Dec 19. <https://doi.org/10.1111/ner.13338>.
- [37] Bermejo P, López M, Larraya I, Chamorro J, Cobo JL, Ordóñez S, Vega JA. Innervation of the human cavum conchae and auditory canal: anatomical basis for transcutaneous auricular nerve stimulation. *Biomed Res Int* 2017;2017:7830919.
- [38] Cook DN, Thompson S, Stomberg-Firestein S, Bikson M, George MS, Jenkins DD, Badran BW. Design and validation of a closed-loop, motor-activated auricular vagus nerve stimulation (MAAVNS) system for neuro-rehabilitation. *Brain Stimul*. 2020;13:800–3.
- [39] Unal G, Swami JK, Canela C, Cohen SL, Khadka N, FallahRad M, Short B, Argyelan M, Sackheim HA, Bikson M. Adaptive current-flow models of ECT: explaining individual static impedance, dynamic impedance, and brain current density. *Brain Stimul* 2021 Jul 28;14(5):1154–68.
- [40] Arlotti M, Rahman A, Minhas P, Bikson M. Axon terminal polarization induced by weak uniform DC electric fields: a modeling study. *nnu Int Conf IEEE Eng Med Biol Soc*. 2012;2012:4575–8.
- [41] Chan CY, Nicholson C. Modulation by applied electric fields of Purkinje and stellate cell activity in the isolated turtle cerebellum. *J Physiol* 1986 Feb;371:89–114.
- [42] Chakraborty D, Truong DQ, Bikson M, Kaphzan H. Neuromodulation of axon terminals. *Cerebr Cortex* 2018 Aug 1;28(8):2786–94.
- [43] Ranck Jr JB. Which elements are excited in electrical stimulation of mammalian central nervous system: a review. *Brain Res* 1975 Nov 21;98(3):417–40.
- [44] Jackson MP, Rahman A, Lafon B, Kronberg G, Ling D, Parra LC, Bikson M. Animal models of transcranial direct current stimulation: methods and mechanisms. *Clin Neurophysiol* 2016 Nov;127(11):3425–54.
- [45] Capogrosso M, Lempka SF. A computational outlook on neurostimulation. *Bioelectr Med* 2020;6:1–7.
- [46] McIntyre CC, Grill WM, Sherman DL, Thakor NV. Cellular effects of deep brain stimulation: model-based analysis of activation and inhibition. *J Neurophysiol* 2004;91:1457–69.
- [47] Mourdoukoutas AP, Truong DQ, Adair DK, Simon BJ, Bikson M. High-resolution multi-scale computational model for non-invasive cervical vagus nerve stimulation. *Neuromodulation: Technol. Neural Interface* 2018;21:261–8.
- [48] Badran BW, Mithoefer OJ, Summer CE, LaBate NT, Glusman CE, Badran AW, DeVries WH, Summers PM, Austelle CW, McTeague LM. Short trains of transcutaneous auricular vagus nerve stimulation (taVNS) have parameter-specific effects on heart rate. *Brain Stimul*. 2018d;11:699–708.
- [49] Scocco R, Garcia RG, Kettner NW, Fisher HP, Isenburg K, Makarovskiy M, Stowell JA, Goldstein J, Barbieri R, Napadow V. Stimulus frequency modulates brainstem response to respiratory-gated transcutaneous auricular vagus nerve stimulation. *Brain Stimul*. 2020;13:970–8.
- [50] Aberra AS, Wang B, Grill WM, Peterchev AV. Simulation of transcranial magnetic stimulation in head model with morphologically-realistic cortical neurons. *Brain Stimul* 2020 Jan-Feb;13(1):175–89.
- [51] Bai S, Loo C, Lovell NH, Dokos S. Comparison of three right-unilateral electroconvulsive therapy montages. *Annu Int Conf IEEE Eng Med Biol Soc*. 2013;2013:819–22.
- [52] Neuling T, Wagner S, Wolters CH, Zaehle T, Herrmann CS. Finite-element model predicts current density distribution for clinical applications of tDCS. *Front Psychiatr* 2012 Sep 24;3:83.
- [53] Seilwinder J, Kammer T, Andrä W, Bellemann ME. A 3D FEM model for calculation of electromagnetic fields in transcranial magnetic stimulation [A 3D FEM model for calculation of electromagnetic fields in transmagnetic stimulation]. *Biomed Tech* 2002;47(Suppl 1 Pt 1):285–8.
- [54] Argyelan M, Oltedal L, Deng ZD, Wade B, Bikson M, Joanlanne A, Sanghani S, Bartsch H, Cano M, Dale AM, Dannowski U, Dols A, Ennekeng V, Espinoza R, Kessler U, Narr KL, Odegaard KJ, Oudega ML, Redlich R, Stek ML, Takamiya A, Emsell L, Bouckaert F, Sienraert P, Pujol J, Tendolkar I, van Eijndhoven P, Petrides G, Malhotra AK, Abbott C. Electric field causes volumetric changes in the human brain. *Elife* 2019 Oct 23;8:e49115.
- [55] Datta A, Baker JM, Bikson M, Fridriksson J. Individualized model predicts brain current flow during transcranial direct-current stimulation treatment in responsive stroke patient. *Brain Stimul* 2011 Jul;4(3):169–74.
- [56] Gunalan K, Howell B, McIntyre CC. Quantifying axonal responses in patient-specific models of subthalamic deep brain stimulation. *Neuroimage* 2018 May 15;172:263–77.
- [57] Huang Y, Liu AA, Lafon B, Friedman D, Dayan M, Wang X, Bikson M, Doyle WK, Devinsky O, Parra LC. Measurements and models of electric fields in the *in vivo* human brain during transcranial electric stimulation. *Elife* 2017 Feb 7;6:e18834.
- [58] Laakso I, Mikkonen M, Koyama S, Hirata A, Tanaka S. Can electric fields explain inter-individual variability in transcranial direct current stimulation of the motor cortex? *Sci Rep* 2019 Jan 24;9(1):626.
- [59] Lempka SF, Zander HJ, Anaya CJ, Wyant A, Ozinga 4th JG, Machado AG. Patient-specific analysis of neural activation during spinal cord stimulation for pain. *Neuromodulation* 2020 Jul;23(5):572–81.
- [60] Paleczny B, Seredyński R, Ponikowska B. Inspiratory-and expiratory-gated transcutaneous vagus nerve stimulation have different effects on heart rate in healthy subjects: preliminary results. *Clin Auton Res* 2019;1–10.
- [61] McNeal DR. Analysis of a model for excitation of myelinated nerve. *IEEE Trans Biomed Eng* 1976 Jul;23(4):329–37.
- [62] Nagarajan SS, Durand DM, Warman EN. Effects of induced electric fields on finite neuronal structures: a simulation study. *IEEE Trans Biomed Eng* 1993 Nov;40(11):1175–88.
- [63] Rattay F, Aberham M. Modeling axon membranes for functional electrical stimulation. *IEEE Trans Biomed Eng* 1993 Dec;40(12):1201–9.
- [64] Warman EN, Grill WM, Durand D. Modeling the effects of electric fields on nerve fibers: determination of excitation thresholds. *IEEE Trans Biomed Eng* 1992 Dec;39(12):1244–54.
- [65] Gaines JL, Finn KE, Slopsema JP, Heyboer LA, Polasek KH. A model of motor and sensory axon activation in the median nerve using surface electrical stimulation. *J Comput Neurosci* 2018 Aug;45(1):29–43.
- [66] Helmers SL, Begnaud J, Cowley A, Corwin HM, Edwards JC, Holder DL, Kostov H, Larsson PG, Levisohn PM, De Menezes MS, Stefan H, Labiner DM. Application of a computational model of vagus nerve stimulation. *Acta Neurol Scand* 2012 Nov;126(5):336–43.
- [67] Johnson MD, Dweiri YM, Cornelius J, Strohl KP, Steffen A, Suurna M, Soose RJ, Coleman M, Rondoni J, Durand DM, Ni Q. Model-based analysis of implanted hypoglossal nerve stimulation for the treatment of obstructive sleep apnea. *Sleep* 2021 Apr 27;44(44 Suppl 1):S11–9.
- [68] Veltink PH, van Veen BK, Struijk JJ, Holsheimer J, Boom HB. A modeling study of nerve fascicle stimulation. *IEEE Trans Biomed Eng* 1989 Jul;36(7):683–92.
- [69] Salkim E, Shiraz A, Demosthenous A. Influence of cellular structures of skin on fiber activation thresholds and computation cost. *Biomed Phys Eng Exp* 2019;5:015015.
- [70] Rubinstein JT. Axon termination conditions for electrical stimulation. *IEEE Trans Biomed Eng* 1993 Jul;40(7):654–63.
- [71] Tranchina D, Nicholson C. A model for the polarization of neurons by extrinsically applied electric fields. *Biophys J* 1986 Dec;50(6):1139–56.
- [72] Badran BW, Jenkins DD, Cook D, Thompson S, Dancy M, DeVries WH, Mappin G, Summers P, Bikson M, George MS. Transcutaneous auricular vagus nerve stimulation-paired rehabilitation for oromotor feeding problems in newborns: an open-label pilot study. *Front Hum Neurosci* 2020;14:77.
- [73] Badran BW, Jenkins DD, DeVries WH, Dancy M, Summers PM, Mappin GM, Bernstein H, Bikson M, Coker-Bolt P, George MS. Transcutaneous auricular vagus nerve stimulation (taVNS) for improving oromotor function in newborns. *Brain Stimul.: Basic, Transl. Clin. Res. Neuromod.* 2018c;11:1198–200.
- [74] Bremer JD, Gurel NZ, Wittbrodt MT, Shandhi MH, Rapaport MH, Nye JA, Pearce BD, Vaccarino V, Shah AJ, Park J. Application of noninvasive vagal nerve stimulation to stress-related psychiatric disorders. *J Personalized Med* 2020;10:119.
- [75] Kong J, Fang J, Park J, Li S, Rong P. Treating depression with transcutaneous auricular vagus nerve stimulation: state of the art and future perspectives. *Front Psychiatr* 2018;9:20.
- [76] Aranow C, Atish-Fregoso Y, Lesser M, Mackay M, Anderson E, Chavan S, Zanos TP, Datta-Chaudhuri T, Bouton C, Tracey KJ. Transcutaneous auricular vagus nerve stimulation reduces pain and fatigue in patients with systemic lupus erythematosus: a randomised, double-blind, sham-controlled pilot trial. *Ann Rheum Dis* 2021;80:203–8.
- [77] Garcia RG, Lin RL, Lee J, Kim J, Barbieri R, Scocco R, Wasan AD, Edwards RR, Rosen BR, Hadjikhani N. Modulation of brainstem activity and connectivity by respiratory-gated auricular vagal afferent nerve stimulation (RAVANS) in migraine patients. *Pain* 2017;158:1461.
- [78] Usichenko T, Hacker H, Lotze M. Transcutaneous auricular vagal nerve stimulation (taVNS) might be a mechanism behind the analgesic effects of auricular acupuncture. *Brain Stimul*. 2017;10:1042–4.
- [79] Zhang Y, Huang Y, Li H, Yan Z, Zhang Y, Liu X, Hou X, Chen W, Tu Y, Hodges S, Chen H, Liu B, Kong J. Transcutaneous auricular vagus nerve stimulation (taVNS) for migraine: an fMRI study. *Reg Anesth Pain Med* 2021;46:145–50.
- [80] Qureshi IS, Datta-Chaudhuri T, Tracey KJ, Pavlov VA, Chen AC. Auricular neural stimulation as a new non-invasive treatment for opioid detoxification. *Bioelectr Med* 2020;6:1–8.
- [81] Baig SS, Falidas K, Laud PJ, Snowdon N, Farooq MU, Ali A, Majid A, Redgrave JN. Transcutaneous auricular vagus nerve stimulation with upper limb repetitive

- task practice may improve sensory recovery in chronic stroke. *J Stroke Cerebrovasc Dis* 2019;28:104348.
- [82] Baptista AF, Baltar A, Okano AH, Moreira A, Campos ACP, Fernandes AM, Brunoni AR, Badran BW, Tanaka C, de Andrade DC. Applications of non-invasive neuromodulation for the management of disorders related to COVID-19. *Front Neurol* 2020;11:1248.
- [83] Bretherton B, Atkinson L, Murray A, Clancy J, Deuchars S, Deuchars J. Effects of transcutaneous vagus nerve stimulation in individuals aged 55 years or above: potential benefits of daily stimulation. *Aging (Albany NY)* 2019;11:4836.
- [84] Kraus T, Kiess O, Hösl K, Terekhin P, Kornhuber J, Forster C. CNS BOLD fMRI effects of sham-controlled transcutaneous electrical nerve stimulation in the left outer auditory canal—a pilot study. *Brain Stimul*. 2013;6:798–804.
- [85] George MS, Caulfield KA, O'Leary K, Badran BW, Short EB, Huffman SM, Li X, Kerns SE, Williams NR. Synchronized cervical VNS with accelerated theta burst TMS for treatment resistant depression. *Brain Stimul* 2020 Sep-Oct;13(5):1449–50.
- [86] Badran BW, Dowdle LT, Mithoefer OJ, LaBate NT, Coatsworth J, Brown JC, DeVries WH, Austelle CW, McTeague LM, George MS. Neurophysiologic effects of transcutaneous auricular vagus nerve stimulation (taVNS) via electrical stimulation of the tragus: a concurrent taVNS/fMRI study and review. *Brain Stimul*. 2018b;11:492–500.
- [87] Frangos E, Ellrich J, Komisaruk BR. Non-invasive access to the vagus nerve central projections via electrical stimulation of the external ear: fMRI evidence in humans. *Brain Stimul*. 2015;8:624–36.
- [88] Yankunina N, Kim SS, Nam EC. Optimization of transcutaneous vagus nerve stimulation using functional MRI. *Neuromodulation: Technol. Neural Interface* 2017;20:290–300.
- [89] Keute M, Machetanz K, Berelidze L, Guggenberger R, Gharabaghi A. Neurocardiac coupling predicts transcutaneous auricular Vagus Nerve Stimulation effects. *Brain Stimul*. 2021;14(2):209–16.
- [90] Charvet LE, Kasschau M, Datta A, Knotkova H, Stevens MC, Alonso A, Loo C, Krull KR, Bikson M. Remotely-supervised transcranial direct current stimulation (tDCS) for clinical trials: guidelines for technology and protocols. *Front Syst Neurosci* 2015;9:26.
- [91] Peterchev AV, Wagner TA, Miranda PC, Nitsche MA, Paulus W, Lisanby SH, Pascual-Leone A, Bikson M. Fundamentals of transcranial electric and magnetic stimulation dose: definition, selection, and reporting practices. *Brain Stimul*. 2012;5:435–53.
- [92] Farmer AD, Strzelczyk A, Finisguerra A, Gourine AV, Gharabaghi A, Hasan A, Burger AM, Jaramillo AM, Mertens A, Majid A, Verkuil B, Badran BW, Venturini-Bort C, Gaul C, Beste C, Warren CM, Quintana DS, Hämmmerer D, Freri E, Frangos E, Tobaldini E, Kaniusas E, Rosenow F, Capone F, Panetsos F, Ackland GL, Kaithwas G, O'Leary GH, Genheimer H, Jacobs HIL, Van Diest I, Schoonen J, Redgrave J, Fang J, Deuchars J, Széles JC, Thayer JF, More K, Vonck K, Steenbergen L, Vianna LC, McTeague LM, Ludwig M, Veldhuizen MG, De Couck M, Casazza M, Keute M, Bikson M, Andreatta M, D'Agostini M, Weymar M, Betts M, Prigge M, Kaess M, Roden M, Thai M, Schuster NM, Montano N, Hansen N, Kroemer NB, Rong P, Fischer R, Howland RH, Scocco R, Sellaro R, Garcia RG, Bauer S, Gancheva S, Stavrakis S, Kampusch S, Deuchars SA, Wehner S, Laborde S, Usichenko T, Polak T, Zaehle T, Borges U, Teckentrup V, Jandackova VK, Napadow V, Koenig J. International Consensus based review and Recommendations for Minimum reporting standards in research on transcutaneous vagus nerve stimulation (version 2020). *Front Hum Neurosci* 2021;14:568051.